FINAL Rec 1 Aug Acc 18 Aug

2

REPORT DOCUMENTATION PAGE

Form Approved
OMB No. 0704-0188

1. AGENCY USE ONLY (Leave Blank)	2. REPORT DATE	3. REPORT TYPE AND DATES COVERED
	29 June 1995	Final Report 30 Sept 94 - 25 June 95

4. TITLE AND SUBTITLE
Modeling and Simulation of CVD Processes for Manufacturing Ceramic Composites

5. FUNDING NUMBERS
Grant number F49620-94-C-0091

6. AUTHOR(S)
S. Adjerid, J.E. Flaherty, J.B. Hudson, and M.S. Shephard
B.E. Webster

AFOSR-TR-95 0643

7. PERFORMING ORGANIZATION NAME(S) AND ADDRESS(ES)
Centric Engineering Systems, Inc.
3393 Octavius Drive Suite 201
Santa Clara, CA 95054-3004

Rensselaer Polytechnic Institute
Troy, NY 12180-3590

8. PERFORMING ORGANIZATION REPORT NUMBER
CVD 062995

9. SPONSORING/MONITORING AGENCY NAME(S) AND ADDRESS(ES)
Dr. James M. McMichael/~~Mr. John Cohan~~
AFOSR/NA
110 Duncan Avenue, Suite B115
Bolling AFB, DC 20332-0001

N A

10. SPONSORING/MONITORING AGENCY REPORT NUMBER
F49620-94-C-0091

11. SUPPLEMENTARY NOTES
*Original contains color plates: All DTIC reproductions will be in black and white.

12a. DISTRIBUTION/AVAILABILITY STATEMENT
Approved for public release, distribution unlimited.

12b. DISTRIBUTION CODE

13. ABSTRACT (Maximum 200 words)

A chemical vapor deposition (CVD) process used to coat crystal sapphire fibers with B-Al_2O_3 has been mathematically modelled and numerically simulated using adaptive finite element software. This software system is applicable for solving transient and steady partial differential equations and is capable of automatic mesh generation, mesh-order variation, and/or mesh refinement. Specifically, for this type of CVD process, the viscous flow system for the carrier gas mixture is coupled with the energy equations for the mixture and the fiber, as well as species equations combined with a surface reaction model and a fiber coating thickness equation. A parameter study of how film coatings and their growth are influenced by various process variables was also accomplished. As a result, this simulation capability demonstrated how it can be used to help design control strategies for optimal coating for production CVD processes.

Future efforts will focus on developing surface reaction models which include multistep and multi-species mixtures, experimental work to understand surface chemistry, simulating coating tows offibers, and integrating the developed CVD modeling/simulation capability into a commercially supported multiphysics s/w package entitled SPECTRUM.

14. SUBJECT TERMS	15. NUMBER OF PAGES
CVD, Ceramic Composites, Crystal Sapphire Fibers, B-Al_2O_3, Adaptive Finite Element Methodology, Parameter Study	25
	16. PRICE CODE

17. SECURITY CLASSIFICATION OF REPORT	18. SECURITY CLASSIFICATION OF THIS PAGE	19. SECURITY CLASSIFICATION OF ABSTRACT	20. LIMITATION OF ABSTRACT
UNCLASSIFIED	UNCLASSIFIED	UNCLASSIFIED	

REF D

DISCLAIMER NOTICE

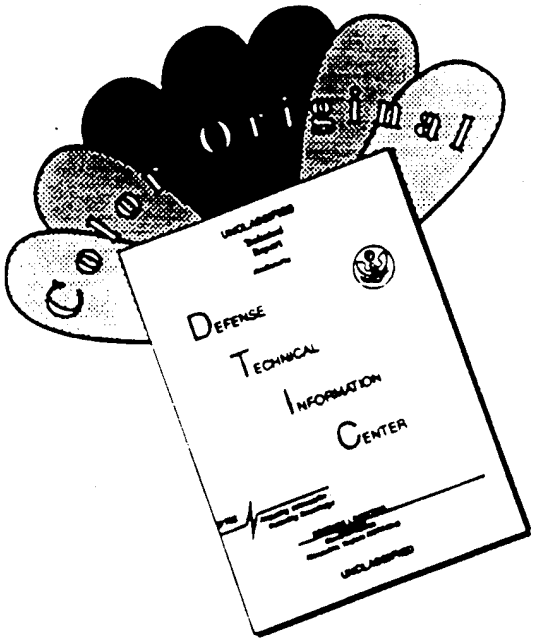

THIS DOCUMENT IS BEST QUALITY AVAILABLE. THE COPY FURNISHED TO DTIC CONTAINED A SIGNIFICANT NUMBER OF COLOR PAGES WHICH DO NOT REPRODUCE LEGIBLY ON BLACK AND WHITE MICROFICHE.

FINAL REPORT
MODELING AND SIMULATION OF CVD PROCESSES FOR MANUFACTURING CERAMIC COMPOSITES
Grant Number F49620-94-C-0091
30 September 1994 - 29 June 1995

S. Adjerid, J. E. Flaherty, J. B. Hudson, and M. S. Shephard

Rensselaer Polytechnic Institute

and

B. Webster

Centric Engineering

1. Introduction. A chemical vapor deposition (CVD) process has been used to coat short length single crystal sapphire fibers with β–Al_2O_3. In order to make the process viable for producing the longer coated fibers needed for practical composite materials, it will be necessary to use a continuous CVD process. This will require the determination of critical parameters and a control strategy for optimal coating.

We have developed a mathematical model of the coating process and used our adaptive finite element software to perform a parameter study of film coatings and their growth rates as functions of operating temperature, precursor mass fraction and distribution, system pressure, flow rate, fiber speed, reaction probability, and reactor geometry. This initial study has helped to determine critical parameters of the process and will help to develop production software.

The system consists of a carrier gas entering at the bottom of a cylindrical hot-wall

reactor containing a single central fiber and exiting at the top. The fiber may be drawn in either the same or the opposite direction as the gas flow. Both the gas mixture and the fiber enter the reactor at ambient temperature. When the flow stablizes, small quantities of the precursor are added to the carrier gas. The gas is heated by a combination of conduction and convection while the fiber is heated by convection and radiation. A thin layer of β–Al_2O_3 coats all heated solid surfaces. Typical values of operating parameters and reactor geometry are given in Table I.

Table I. Typical Operating Parameters and Reactor Geometry.

Reactor diameter	2.5 *cm*
Reactor length	1 *m*
Fiber diameter	40 μm
Oxygen flow rate	250 *scc* /min
Argon flow rate	100 *scc /min*
Outlet pressure	10–20 *torr*
Reactor Temperature	900°*C*

2. Mathematical Model. We model the system as a three-dimensional axisymmetric steady flow of an ideal gas. As an initial step, we neglect reactions in the fluid, the effect of the deposited films on the fluid flow, thermal diffusion, and the heat released by surface reactions. We further assume that every precursor molecule that collides with the wall or the fiber surface has a probability α* of reacting and depositing Al_2O_3 on the surface and that inert products are carried away by the flow. At any instant, the mixture contains only oxygen, argon, and precursor which are indexed by $i = 1, 2, 3$, respectively. The deposited Al_2O_3 is indexed by $i = 4$. Let Y_i and x_i, respectively, denote the mass and mole fractions of species $i = 1, 2, 3$, present in the gas mixture and M_i denote the molecular weight of species $i = 1, 2, 3, 4$.

2.1. Fluid Flow. The mathematical model [1,2] of the gaseous mixture in cylindrical coordinates (r, z), consists of

* A list of symbols appears in Table II near the end of this report

(i) a continuity equation

$$\frac{1}{r}\frac{\partial(r\rho v_r)}{\partial r} + \frac{\partial(\rho v_z)}{\partial z} = 0, \tag{2.1}$$

(ii) momentum equations

$$\rho\left[v_r\frac{\partial v_r}{\partial r} + v_z\frac{\partial v_r}{\partial z}\right] = -\frac{\partial p}{\partial r} + \left[\frac{1}{r}\frac{\partial(r\tau_{rr})}{\partial r} - \frac{\tau_{\phi\phi}}{r} + \frac{\partial\tau_{rz}}{\partial z}\right], \tag{2.2a}$$

$$\rho\left[v_r\frac{\partial v_z}{\partial r} + v_z\frac{\partial v_z}{\partial z}\right] = -\frac{\partial p}{\partial z} + \left[\frac{1}{r}\frac{\partial(r\tau_{rz})}{\partial r} + \frac{\partial\tau_{zz}}{\partial z}\right] - \rho g, \tag{2.2b}$$

(iii) stress tensor components

$$\tau_{rr} = \frac{2}{3}\mu\left[2\frac{\partial v_r}{\partial r} - \frac{v_r}{r} - \frac{\partial v_z}{\partial z}\right], \qquad \tau_{\phi\phi} = \frac{2}{3}\mu\left[-\frac{\partial v_r}{\partial r} + 2\frac{v_r}{r} - \frac{\partial v_z}{\partial z}\right], \tag{2.2c,d}$$

$$\tau_{rz} = \mu\left[\frac{\partial v_r}{\partial z} + \frac{\partial v_z}{\partial r}\right], \qquad \tau_{zz} = \frac{2}{3}\mu\left[2\frac{\partial v_z}{\partial z} - \frac{v_r}{r} - \frac{\partial v_r}{\partial r}\right], \tag{2.2e,f}$$

(iv) an energy equation

$$c_p\rho\left[v_r\frac{\partial T}{\partial r} + v_z\frac{\partial T}{\partial z}\right] = \left[\frac{1}{r}\frac{\partial}{\partial r}\left[rk\frac{\partial T}{\partial r}\right] + \frac{\partial}{\partial z}\left[k\frac{\partial T}{\partial z}\right]\right], \tag{2.3}$$

(v) a reacting species transport equation

$$\rho\left[v_r\frac{\partial Y_3}{\partial r} + v_z\frac{\partial Y_3}{\partial z}\right] = \left[\frac{1}{r}\frac{\partial}{\partial r}\left[r\rho D\frac{\partial Y_3}{\partial r}\right] + \frac{\partial}{\partial z}\left[\rho D\frac{\partial Y_3}{\partial z}\right]\right], \tag{2.4}$$

and (vi) an equation of state

$$\rho = \frac{\overline{M}p}{R_g T}. \tag{2.5b}$$

The quantities v_r and v_z are the radial and axial components of the mixture velocity **v**, p is the pressure, T is the temperature, ρ is mixture density, μ is the mixture viscosity, k is the mixture thermal conductivity, g is gravitational acceleration, c_p is the mixture specific heat, D is the precursor diffusivity in the mixture, R_g is the universal gas constant, and $\overline{M}$ is the mixture mean molecular weight given by

$$\overline{M} = \sum_{i=1}^{2} x_i M_i, \tag{2.5b}$$

assuming $x_3 << x_i$, $i = 1, 2$.

2.2. Surface Reaction and Film Growth. As a first approximation in modeling the complex surface reaction, we have assumed that every precursor molecule that hits the surface reacts according to

$$2\,(Al\text{–}(O\text{–}C_2H_5)_3)_{gas} + 3\,(O_2)_{gas} \longrightarrow (Al_2O_3)_{solid} + 6\,(C_2H_2)_{gas} + 9\,(H_2O)_{gas}, \tag{2.6a}$$

to deposit the desired material. By-products of this reaction are assumed to be inert and carried away by the flow. The impingement rate I of the precursor in the mixture is the number of molecules of this species that hit the surface per unit area per unit time, i.e.,

$$I = \frac{px_3}{\sqrt{2\pi m_3 \kappa T}} \tag{2.6b}$$

where κ is Boltzmann's constant and m_3 is the mass per molecule of the precursor. Assuming the flux I_r of precursor reacting on the solid surfaces to be proportional to the impingement rate I and the reaction probability $\alpha(T)$, and using $\kappa = R_g/N_{Av}$ and the mixture relation [6]

$$x_3 = \frac{Y_3/M_3}{\sum_{j=1}^{3} Y_j/M_j} \tag{2.6c}$$

with $x_3 \ll x_j$, $j = 1, 2$, we obtain

$$I_r = \beta\,\alpha(T)\,\frac{Y_3 p}{\sqrt{T}}, \tag{2.7a}$$

where

$$\beta = \frac{(\overline{M}/M_3)}{\sqrt{2\pi M_3 R_g}}, \quad \alpha(T) = Ae^{-\frac{\Delta H}{T}}, \tag{2.7b,c}$$

and the activation energy ΔH and A are to be selected (see Section 4).

We denote the thickness of the film on the fiber surface by $h(z)$ and use (2.7) to obtain

$$\frac{\partial h}{\partial z} v_f - 1/2 M_4 \frac{I_r}{\rho_4} = 0, \quad 0 \le z \le L, \tag{2.8}$$

where ρ_4 is the density of Al_2O_3 and L is the reactor length.

2.3. Boundary Conditions. The system (2.1-8) is closed by adding boundary conditions at the inlet, outlet, wall, and fiber surface. We consider cases involving (i) flow in the whole reactor and (ii) flow in the central part of the furnace.

2.3.1. Whole Reactor Boundary Conditions. To determine the flow in the entire tube, we solve (2.1-8) subject to the following conditions:

(i) at the inlet

$$v_r = 0,\ v_z = v_{in},\ T = T_{in},\ Y_3 = w_{in},\ p = p_{in},\quad at\ z = 0,\ R_f \le r \le R, \tag{2.9a,b,c,d,e}$$

(ii) on the wall

$$v_r = 0,\ v_z = 0,\ T = T_w(z),\ D\rho\frac{\partial Y_3}{\partial r} = M_3 I_r,\ at\ r = R,\ 0 \le z \le L, \tag{2.9f,g,h,i}$$

(iii) at the outlet

$$\frac{\partial v_r}{\partial z} = 0,\ \frac{\partial v_z}{\partial z} = 0,\ \frac{\partial T}{\partial z} = 0,\ \frac{\partial Y_3}{\partial z} = 0,\ at\ z = L,\ R_f \le r \le R, \tag{2.9j,k,l,m}$$

and (iv) on the fiber

$$v_r = 0,\ v_z = v_f,\ \rho D\frac{\partial Y_3}{\partial r} = M_3 I_r,\ h(0) = 0, \tag{2.9n,o,p,q}$$

$$\rho_f c_{pf}\frac{\partial T}{\partial z}v_f - \frac{\partial}{\partial z}(k_f\frac{\partial T}{\partial z}) - f_c = 0,\ T(R_f, 0) = T_{in}(R_f),\ \frac{\partial T}{\partial z}(R_f, L) = 0,\quad at\ r = R_f,\ 0 \le z \le L, \tag{2.9r,s,t}$$

where radiant heat flux from the wall is neglected, $f_c = k\partial T/\partial r$ is the convective heat flux from the gas to the fiber, and R_f and R_w are the fiber and reactor radii, respectively. Heat conduction in the fiber is modeled by the one-dimensional heat conduction equation (2.9r,s,t) which is coupled to the gas energy equation through f_c. The quantities ρ_f, c_{pf}, k_f, and v_f denote the fiber density, specific heat, thermal conductivity, and velo-

city, respectively, while v_{in}, T_{in}, p_{in}, w_{in} are the axial velocity, the temperature, the pressure, and the precursor mass fraction at the inlet of the reactor, respectively.

2.3.2. Central Core Boundary Conditions. Assuming the flow to reach a constant temperature $\bar{T}$ away from the inlet and outlet, the density becomes constant in the central part of the furnace. Therefore, we model the central part of the CVD reactor by (2.1-2), (2.4-8) subject to the boundary conditions:

(i) at the inlet

$$v_r = 0, \quad v_z = v_{in}, \; Y_3 = w_{in}, \; p = p_{in}, \; at \; z = 0, \quad R_f \le r \le R, \qquad (2.10a,b,c,d)$$

(ii) on the wall

$$v_r = 0, \quad v_z = 0, \; \rho D \frac{\partial Y_3}{\partial r} = M_3 I_r, \; at \quad r = R, \quad 0 \le z \le L, \qquad (2.10e,f,g)$$

(iii) at the outlet

$$\frac{\partial v_r}{\partial z} = 0, \quad \frac{\partial v_z}{\partial z} = 0, \quad \frac{\partial Y_3}{\partial z} = 0, \quad at \quad z = L, \quad R_f \le r \le R, \qquad (2.10h,i,j)$$

and (iv) on the fiber

$$h(z_{in}) = 0, \; v_r = 0, \quad v_z = v_f, \quad \rho D \frac{\partial Y_3}{\partial r} = M_3 I_r,$$
$$at \quad r = R_f, \; 0 \le z \le L. \qquad (2.10k,l,m,n)$$

2.4 Physical Properties. Evaluation of physical properties of the gas mixture is performed using experimental tables and mixture theory [6] assuming an argon and oxygen mixture, i.e., $x_3 \approx 0$. The mixture viscosity, thermal diffusivity, and specific heat are given by

$$\mu = \sum_{i=1}^{2} \frac{x_i \mu_i}{\sum_{j=1}^{2} x_j \phi_{ij}}, \quad k = \sum_{i=1}^{2} \frac{x_i k_i}{\sum_{j=1}^{2} x_j \phi_{ij}}, \quad c_p = \sum_{i=1}^{2} Y_i c_{pi}, \qquad (2.11a,b,c)$$

with

$$\phi_{ij} = \frac{\left[1+\left(\mu_i/\mu_j\right)^{1/2}\left(M_j/M_i\right)^{1/4}\right]^2}{\sqrt{8}[1 + (M_i/M_j)]^{1/2}}, \tag{2.11d}$$

where μ_i, k_i, and c_{pi} denote the viscosity, thermal conductivity, and specific heat, respectively, of species $i = 1, 2$.

Using a least-squares fit to the data generated from (2.11) and the experimental tables [6], we obtain

$$\mu(T) = 10^{-5}(0.351796 + 0.68085210^{-2}\,T - 0.301185510^{-5}\,T^2 + 0.818010710^{-9}\,T^3),$$

$$c_p(T) = 10^3(0.727147 + 0.19714910^{-3}\,T - 0.654446410^{-9}\,T^2 - 0.26141910^{-10}\,T^3),$$

$$k(T) = 10^{-2}(0.308270 + 0.75678010^{-6}\,T - 0.139484010^{-9}\,T^2). \tag{2.12a,b,c}$$

The diffusion coefficient of precursor in a mixture of oxygen and argon is computed using the binary diffusion theory [6]

$$D = (8R_g/\pi)^{3/2}\frac{N_{Av}}{3\delta}\frac{\sqrt{T^3(1/M_3+1/\bar{M})}}{p}. \tag{2.12d}$$

We estimate the collision diameter $\delta = 12.5\,10^{-10}m$ to obtain

$$D = c_d\frac{T^{3/2}}{p}, \text{ with } c_d = 2.5610^{-5} \tag{2.12e}$$

3. Numerical Solution Procedure.. We obtain a dimensionless version of (2.1-10) by using

$$r = \bar{L}\tilde{r},\ z = \bar{L}\tilde{z},\ T = \bar{T}\tilde{T},\ v_r = \bar{U}\tilde{v}_r,\ v_z = \bar{U}\tilde{v}_z,\ Y_3 = \bar{W}\tilde{Y}_3,\ p = \bar{\rho}\bar{U}^2\tilde{p},$$

$$h = \bar{H}\tilde{h},\ k = \bar{k}\tilde{k},\ D = \bar{D}\tilde{D},\ c_p = \bar{c}_p\tilde{c}_p, \text{ and } \mu = \bar{\mu}\tilde{\mu}, \tag{3.1a}$$

where

$$\bar{T} = T_{in},\ \bar{L} = L,\ \bar{W} = 1,\ \bar{\rho} = \rho(T_{in}, p_{in}),\ \bar{H} = 1m,\ \bar{k} = k(T_{in}),\ \bar{c}_p = c_p(T_{in}),$$

$$\bar{\mu} = \mu(T_{in}), \text{ and } \bar{D} = D(T_{in}, p_{in}) \tag{3.1b}$$

In the remainder of this report, we consider the dimensionless system and omit the ˜.

3.1 Stabilization Method. Since standard Galerkin finite-element methods based on equal polynomial degrees for both velocity and pressure fail to satisfy the Babuska-Brezzi stability condition [4], we implemented the Douglas-Wang stabilized streamline upwind method [5] that consists of perturbing the standard finite element formulation by the elemental least-squares term

$$\phi_h = \sum_{K=1}^{N_\Delta} \Big(\mathbf{R}[\mathbf{v}_h, p_h], c_k(\mathbf{v}_h)\, \mathbf{A}[\mathbf{v}_h](q_h, \mathbf{w}_h) \Big)_K, \tag{3.2a}$$

where the L_2 inner product on element K is

$$(\phi, \psi)_K = \int_K \phi\psi dK,$$

$\mathbf{v}_h$ and $\mathbf{w}_h$ denote trial and test functions, respectively, for the velocity; p_h and q_h denote the trial and test functions, respectively, for the pressure; $\mathbf{R}[\mathbf{v}, p]$ is the residual

$$\mathbf{R}[\mathbf{v}, p] = \begin{bmatrix} \rho\left(v_r \dfrac{\partial v_r}{\partial r} + v_z \dfrac{\partial v_r}{\partial z}\right) + \dfrac{\partial p}{\partial r} - \dfrac{1}{\mathrm{Re}}\left[\dfrac{1}{r}\dfrac{\partial (r\tau_{rr})}{\partial r} - \dfrac{\tau_{\phi\phi}}{r} + \dfrac{\partial \tau_{rz}}{\partial z}\right] \\ \rho\left(v_r \dfrac{\partial v_z}{\partial r} + v_z \dfrac{\partial v_z}{\partial z}\right) + \dfrac{\partial p}{\partial z} - \dfrac{1}{\mathrm{Re}}\left[\dfrac{1}{r}\dfrac{\partial (r\tau_{rz})}{\partial r} + \dfrac{\partial \tau_{zz}}{\partial z}\right] + \dfrac{\rho}{Fr} \end{bmatrix}, \tag{3.2b}$$

where $\mathrm{Re} = \bar{\rho}\bar{U}\bar{L}/\bar{\mu}$ is Reynolds number, and $Fr = \bar{U}^2/(g\bar{L})$ is Froud number. Finally, the operator $\mathbf{A}[\mathbf{v}_h]$ is given by

$$\mathbf{A}[\mathbf{v}](q, \mathbf{w}) = \begin{bmatrix} \rho\left(v_r \dfrac{\partial w_r}{\partial r} + v_z \dfrac{\partial w_r}{\partial z}\right) - \dfrac{\partial q}{\partial r} + \gamma \dfrac{1}{\mathrm{Re}}\left[\dfrac{1}{r}\dfrac{\partial (r\tilde{\tau}_{rr})}{\partial r} - \dfrac{\tilde{\tau}_{\phi\phi}}{r} + \dfrac{\partial \tilde{\tau}_{rz}}{\partial z}\right] \\ \rho\left(v_r \dfrac{\partial w_z}{\partial r} + v_z \dfrac{\partial w_z}{\partial z}\right) - \dfrac{\partial q}{\partial z} + \gamma \dfrac{1}{\mathrm{Re}}\left[\dfrac{1}{r}\dfrac{\partial (r\tilde{\tau}_{rz})}{\partial r} + \dfrac{\partial \tilde{\tau}_{zz}}{\partial z}\right] \end{bmatrix}, \tag{3.2c}$$

where $\tilde{\tau}_{zz}$, $\tilde{\tau}_{rr}$, $\tilde{\tau}_{rz}$, and $\tilde{\tau}_{\phi,\phi}$ are obtained from equations (2.2c-f) with $\mathbf{v}$ replaced by $\mathbf{w}_h$ and $\gamma = -1$. There are two other popular choices of γ: the choice $\gamma = 0$ yields the Streamline Upwind Petrov-Galerkin (SUPG) method [7,8] and $\gamma = 1$ yields the Galerkin-Least-Squares method [9].

Letting h_K be the diameter of element K and following Franca and Frey [7] yields

$$c_K(\mathbf{v}) = 0.01\,\tau_K, \quad \text{with} \quad \tau_K = \frac{h_K}{2|\mathbf{v}_h|_2}\,\xi(RE_K) \tag{3.2d,e}$$

where

$$|\mathbf{v}|_2 = (v_r^2 + v_z^2)^{1/2},\ RE_K = \frac{RE\,|\mathbf{v}|_2 h_k}{12},\ \text{and}\ \xi(RE_K) = \begin{cases} RE_K, \text{ if } 0 \le RE_K < 1 \\ 1, \text{ if } RE_K \ge 1. \end{cases} \tag{3.1f,g,h}$$

3.2 Adaptive Software. The resulting system modeling the reaction, convection, and diffusion occurring during the CVD processing is solved using adaptive software that can reduce computational difficulties while automating many of the decisions associated with a numerical solution. Our adaptive system has capabilities for automatic quadtree-structured mesh generation, mesh refinement/coarsening (h-refinement), method order variation (p-refinement), and mesh motion (r-refinement); however, only h-refinement was used in this initial study. The mesh is organized in a tree structure where the root node is the domain having as offspring all elements of a base mesh. An error indicator is associated with each quadrilateral element and h-refinement is used to refine those elements having large errors. Elements may be divided into four sub-elements and these are regarded as offspring of their coarser parents in the tree structure. Leaf nodes of the tree represent the actual elements of the mesh. Solutions of two-dimensional stationary and transient problems begin with a trial solution computed on a coarse mesh using a first-order method. The solution is halted periodically and an estimate of the discretization error is appraised. Meshes are subdivided in high-error regions in an attempt to maintain the error estimate within prescribed limits. Estimates of spatial discretization errors are obtained from jumps in gradients of the finite element solution at inter-element boundaries [3].

4. Computational Results

The adaptive software system described in Section 3 has been used to solve a dimensionless version of (2.1-10) using a piecewise bilinear finite element solution on quadrilateral meshes. The initial base mesh was graded near the fiber and the wall to improve the

convergence rate in boundary layers. A 25×25 base mesh was used with up to four levels of refinement. The resulting discrete systems were solved using a quasi-Newton iteration procedure for steady systems or the backward-difference software DASSL for transient systems [10]. In all cases, we selected $Y_1 = 0.667$, $Y_2 = 0.333$, and 40μ diameter fibers drawn at $10^{-4} m/sec$.

4.1. Nonisothermal Case. First, we present results for the whole furnace using (2.1-9). We chose $L = 30cm$, $R = 1cm$, $p = 10\,torr$, $dev = 0.3$, $w = 0.05$, $T_{in} = 300K$, $\bar{T}_w = 1200K$,

$$T_w(z) = T_{in} + (\bar{T}_w - T_{in})\, s(z) \tag{4.1a}$$

with

$$s(z) = \frac{1}{4}\{1 + \tanh[50(z - 0.2)]\}\,\{1 - \tanh[50(z - 0.05)]\}, \tag{4.1b}$$

and a reaction probability

$$\alpha(T) = 0.02\, e^{\frac{\Delta H}{1200}}\, e^{-\frac{\Delta H}{T}}, \text{ with } \Delta H = 10^4. \tag{4.2}$$

The resulting pressure, axial velocity, temperature, and precursor mass fraction are shown in Figure 1. The gas and the fiber reach the wall temperature in the central part of the furnace. As the gas is heated it accelerates in the central part of the furnace. We also present the fiber coating thickness and deposition rates on the wall as function of z in Figure 2. In the preheat zone near the inlet, little if any coating results; however, as soon as the gas reaches the heated zone, surface reactions are triggered and the deposition rate increases to reach a maximum and subsequently decays as the precursor is depleted. As a result of these computations, it appears that the exponential dependence of α on temperature leads to negligible surface reactions for $T < \bar{T}$. We thus decided to simplify this initial study and confine our attention to the central part of the reactor.

4.2. Isothermal Case. We consider the central part of the furnace and perform a parametric study by solving the system (2.1-2), (2.4-8), (2.10) assuming the wall, fiber,

and gas to be at uniform temperature. We consider cases where the precursor is injected near the fiber surface. Let $F_f = m_f/m_{in}$, $F_w = m_w/m_{in}$, and $F_o = m_o/m_{in}$ denote the percentage of precursor that deposits on the fiber, deposits on the wall, and leaves the furnace unreacted, respectively. Here, m_{in} denotes the precursor mass flux entering the furnace, m_f the precursor mass flux depositing on the fiber, m_w the precursor mass flux depositing on reactor walls, and m_o the unreacted precursor mass flux exiting the furnace. We use the percentage F_f of precursor that deposits on the fiber to measure the efficiency of the system. The production rate is measured by the fiber coating thickness at the outlet. At the inlet, the precursor is injected within a distance $dev*(R-R_f)$ of the fiber surface and w_{in} is given by

$$w_{in}(r) = \frac{w}{2}\{1 - \tanh[\varepsilon(r - (R_f + (R_w - R_f)dev))]\}, \text{ with } \varepsilon = \frac{20}{R_w - R_f}. \quad (4.3)$$

Thus, when $dev = 1$, the precursor fraction is uniform at the inlet, and when $dev = 0.5$ the precursor is concentrated within a distance $(R-R_f)/2$ of the fiber.

In order to examine the effect of flow-rate variations on efficiency and production rate of the coating process, we solved (2.1-2), (2.4-8), (2.10) for $p = 20torr$, $\alpha = 0.02$, $R = 1cm$, $L = 20cm$, $w = 0.05$, $T = 1200K$, $dev = 0.05$, and flow rates of 61, 124, 188, 251, 315, $442scc/min$. The results are shown in Figure 3. Higher flow rates yield lower efficiency and higher production rates.

In order to examine the effect of precursor distribution, we solve the system (2.1-2), (2.4-8), (2.10) with $p = 20torr$, $\alpha = 0.05$, $R = 1cm$, $L = 20cm$, $w = 0.05$, $T = 1200K$, and $dev = 0.05$, 0.1, 0.2, 0.3, 0.4 , 0.5 , 0.6, 0.9, with a flow rate of $442scc/min$. The results, shown in Figure 4, indicate that the closer the precursor to the fiber the more efficient the system. This is expected because the precursor has to diffuse further to reach the wall. However, smaller values of dev with a constant w and flow rate, lead to smaller mass fluxes of precursor at the inlet; thus, slower production rates arise (see Figure 4, left).

In order to examine the effect of reactor length, we solved the system (2.1-2), (2.4-8), (2.10) for $p = 20torr$, $\alpha = 0.02$, $R = 1cm$, $w = 0.05$, $dev = 0.1$, $T = 1200K$, a flow rate of $124scc/min$, and $L = 10,\ 20,\ 30,\ 40,\ 50cm$. The results presented in Figure 5 show that longer reactors improve both efficiency and production rate. However, we expect that for a given flow rate, temperature, pressure, and reaction probability, we can determine the optimal reactor length.

In order to examine the effect of reaction probability α, we set $p = 20torr$, $R = 1cm$, $L = 20cm$, $dev = 0.2$, $w = 0.05$, $T = 1200K$, a flow rate of $124scc/min$, with $\alpha = 0.001,\ 0.01,\ 0.05,\ 0.1$ and solve the system (2.1-2), (2.4-8), (2.10). We plot P_w, P_f, and P_o vs. reaction probability α and the coating thickness h as a function of z in Figure 6. These results indicate that for large reaction probabilities the precursor reacts quickly on the fiber surface as it enters the reactor and, therefore, only a small percentage of it reaches the wall or is convected out of the reactor. Thus, a higher reaction probability increases efficiency and production rate.

In order to examine the effects of precursor fraction, we solve the system (2.1-2), (2.4-8), (2.10) for $p = 20torr$, $\alpha = 0.02$, $R = 1cm$, $L = 20cm$, $dev = 0.2$, $T = 1200K$, and a flow rate of $633scc/min$, with $w = 0.05,\ 0.1,\ 0.2,\ 0.5$. The computational results predict that efficiency is independent of precursor mass fraction for a fixed distribution (see Figure 7, left). However, production rate depends linearly on precursor mass fraction.

In order to examine the effect of reactor radius, we assumed the precursor to be injected within a fixed distance from the fiber for all values of R_w and chose $dev = 0.02\,(0.5 - R_f)/(R_w - R_f)$. The other parameters are $p = 20torr$, $\alpha = 0.02$, $w = 0.05$, $L = 20cm$, $T = 1200K$, a flow rate of $350scc/min$ and $R_w = 0.5,\ 1,\ 1.5$. The results, shown in Figure 8, suggest that efficiency and production rate of this CVD process are improved by making the reactor wall farther away from the fiber. The flow velocity decreases with increasing R_w, when holding dev and w fixed. This leads to

a lower precursor flux entering the reactor. Consequently, the production rate of the process deteriorates (see Figure 7, right). Varying the reactor radius produces the same effect as varying dev.

In order to examine the effect of temperature, we assumed a temperature-independent reaction probability $\alpha = 0.02$ and selected $p = 10torr$, $R = 1cm$, $L = 20cm$, $dev = 0.3$, a flow rate of $350scc/min$, and $T = 800, 900, 1000, 1100, 1200, 1300K$. Results, shown in Figure 9 (left), suggest that efficiency is temperature independent. Higher temperatures help precursor molecules diffuse faster towards the walls and deposit before depositing on the fiber or exiting the furnace (see Figure 9, left). The results, shown in Figure 9 (right), indicate that production rates decrease with increasing temperature.

We examine the effect of pressure on the CVD process by solving the partial differential system (2.1-2), (2.4-8), (2.10) with $\alpha = 0.001$, $R = 1cm$, $L = 20cm$, $dev = 0.3$, $T = 1200K$, a flow rate of $350scc$, and chose $p = 2, 5, 10, 15, 20torr$. Our model predicts that higher pressure improve the efficiency of the CVD system (see Figure 10, left). Since the mass flow rate is kept constant, higher pressure with constant temperature yield slower flow, higher impingement rate, and slower diffusion rate. The diffusion rate and the impingement rate cancel; thus, this has the same effects as varying the flow rate.

In order to examine the effect of temperature at constant dwell time, we selected $p = 10torr$, $\alpha = 0.002$, $R = 1cm$, $L = 20cm$, $dev = 0.3$, determined a flow rate to maintain a constant dwell time of $0.05sec$, and solved the system (2.1-2), (2.4-8), (2.10) for $T = 800, 900, 1000, 1100, 1200, 1300K$. Constant reaction probability leads to small variations in efficiency (see Figure 11, left). This happens because of the diffusivity increase with temperature. Higher temperatures lead to a lower density and precursor flux entering the reactor; thus, to a lower production rate (see Figure 11, right).

In order to examine the effect of reactor length at constant dwell time, we chose $p = 20torr$, $\alpha = 0.02$, $R = 1cm$, $w = 0.05$, $dev = 0.3$, $T = 1200K$, a flow rate determined to maintain a constant dwell time of $0.05sec$, and $L = 10, 20, 30, 40, 50, 60cm$. With constant temperature and pressure, results of Figure 12 indicate that efficiency remains constant while the production rate increases with L. We show the axial velocity component v_z for $L = 60cm$ using a 20×20 coarse mesh Figure 13 (top-left) and using a mesh with 3 levels of h-refinement in Figure 13 (top-right). We show a blow-up of the left-lower corner of Figure 13 (top-right) to show the locally refined mesh that improves the accuracy of the numerical solution.

5. Discussion of Results. We have developed a mathematical model to analyze and simulate CVD fiber coating processes for manufacturing ceramic composites. The model is used with a general-purpose adaptive software system for transient and steady partial differential equations that is capable of automatic mesh generation, mesh-order variation, and/or mesh refinement. The viscous flow system for the mixture is coupled with energy equations for the mixture and fiber, a species equations combined with a surface reaction model, and a fiber coating thickness equation. This model has predicted the effects of operating parameters such as temperature, flow rate, pressure, etc. on efficiency and production rates of the CVD process. This model can be easily altered to include other effects such as thermal diffusion, multiple species, multi-step surface reactions, and cold-wall furnaces where the fiber is heated by, e.g., electrical current.

Concentrating the precursor near the fiber and away from the hot wall is the only strategy that substantially improves the efficiency of this hot wall CVD reactor. Higher reaction probabilities yield higher efficiencies, especially when the precursor enters near the fiber. Longer dwell times, controlled by either reactor length or flow rate, permit the precursor to react and deposit on solid surfaces and, thus, improve the production rate rate. While they reduce efficiency, both higher flow rates and precursor concentrations increase the CVD process production rate.

Future efforts will develop a more realistic surface reaction model to include mutli-step and multi-species mixtures. This will be combined with more experimental work to understand the surface chemistry. We will also concentrate our effort on developing a model for a more practical situation of coating tows of fibers. The gas infiltration into the tow becomes important to obtain uniform coatings. Usually, when coating a tow of fibers, the precursor reacts on accessible surfaces of the tow and closes the pores and, thus, prevents further infiltration of the precursor into the interior. We plan to simulate and analyze pore closing. Software for three-dimensional parallel adaptive computations will also be developed. By Combining experimental and state-of-art computational adaptive software, we hope to identify and verify optimal configurations and manufacturing processes much more rapidly than would be possible by using either paradigm alone.

References

[1] Adjerid, S., Flaherty, J.E., Hudson, J.B., and Shephard, M.S., Single crystal sapphire coating via chemical vapor deposition, Progress Report 1, Grant Number F49620-94-C-0091, Modeling and Simulation of CVD Processes for Manufacturing Ceramic Composites (1994).

[2] Adjerid, S., Flaherty, J.E., Hudson, J.B., and Shephard, M.S., Single crystal sapphire coating via chemical vapor deposition, Progress Report 2, Grant Number F49620-94-C-0091, Modeling and Simulation of CVD Processes for Manufacturing Ceramic Composites (1994).

[3] Adjerid, S., Flaherty, J.E., Moore, P.K., and Wang, Y.J., High-order methods for parabolic systems, *Physica D*, 60, 94-111 (1992).

[4] Brezzi, F. and Fortin, M., *Mixed and Hybrid Finite Element Methods*, Springer Verlag, New York (1991).

[5] Douglas, J.,Jr. and Wang, J., An absolutely stabilized finite element method for

Table II. List of Symbols and Parameters.

r, z	Radial and vertical coordinates, respectively
ρ	Mixture density
ρ_4	Density of Al_2O_3
ρ_f	Fiber density
p	Pressure
v_r	Radial component of the velocity
v_z	Axial component of the velocity
T	Temperature
g	Gravitational acceleration
R_g	Universal gas constant
κ	Boltzmann constant
N_{av}	Avogadro number
μ_i	Viscosity of species i
μ	Mixture viscosity
c_{pi}	Specific heat of species i
c_p	Specific heat of the gas mixture
c_{pf}	Fiber specific heat
k	Mixture thermal diffusivity
k_i	Thermal diffusivity of species i
k_f	Fiber thermal diffusivity
D	Precursor diffusivity in the mixture
M_i	Molecular weight of species i
x_i	Mole fraction of species in the mixture
Y_i	Mass fraction of species i in the mixture
w_{in}	Precursor mass fraction at inlet
p_{in}	Pressure at inlet
T_{in}	Temperature at inlet
T	Temperature at central part of the reactor wall
V_{in}	Axial velocity at inlet
M	Mean molecular weight of the mixture
R_f	Fiber radius
R_w	Reactor radius
Re	Reynolds number
Fr	Froud number
ΔH	Surface reaction activation energy
F_f	Percentage of precursor hat deposits on the fiber
F_o	Percentage of unreacted precursor
F_w	Percentage of precursor that deposits on the wall

the Stokes problem, *Math. Comput.*, 52, 495-508 (1989).

[6] Edwards, D.K., Denny, V.E., and Mills, A.F., *Transfer Processes: An Introduction to Diffusion, Convection, and Radiation*, Series in Thermal and Fluids Engineering, Mac Graw Hill, (1979)

[7] Franca, L.P. and Frey, S.L., Stabilized finite element methods: II. The incompres-

sible Navier-Stokes equations, *Comput. Methods in Appl. Mech. and Engrg.,* 99, 209-233 (1991).

[8] Hughes, T.J.R. and Franca, L.P., A new finite element formulation for computational fluid dynamics: VII The Stokes problem with various well-posed boundary conditions: symmetric formulations that converge for all velocity/pressure spaces, *Comput. Methods Appl. Engrg.,* 65, 85-96 (1987).

[9] Hughes, T.J.R., Franca, L.P., and Balestra M., A new finite element formulation for computational fluid dynamics: V Circumventing the Babuska-Brezzi condition: a stable Petrov-Galerkin formulation of the Stokes problem accommodating equal-order interpolations, *Comput. Methods Appl. Engrg.,* 59, 85-99 (1986).

[10] Petzold, L.R., A description of DASSL: a differential/algebraic system solver, Rep. Sand 82-8637 Sandia National Laboratory (1982).

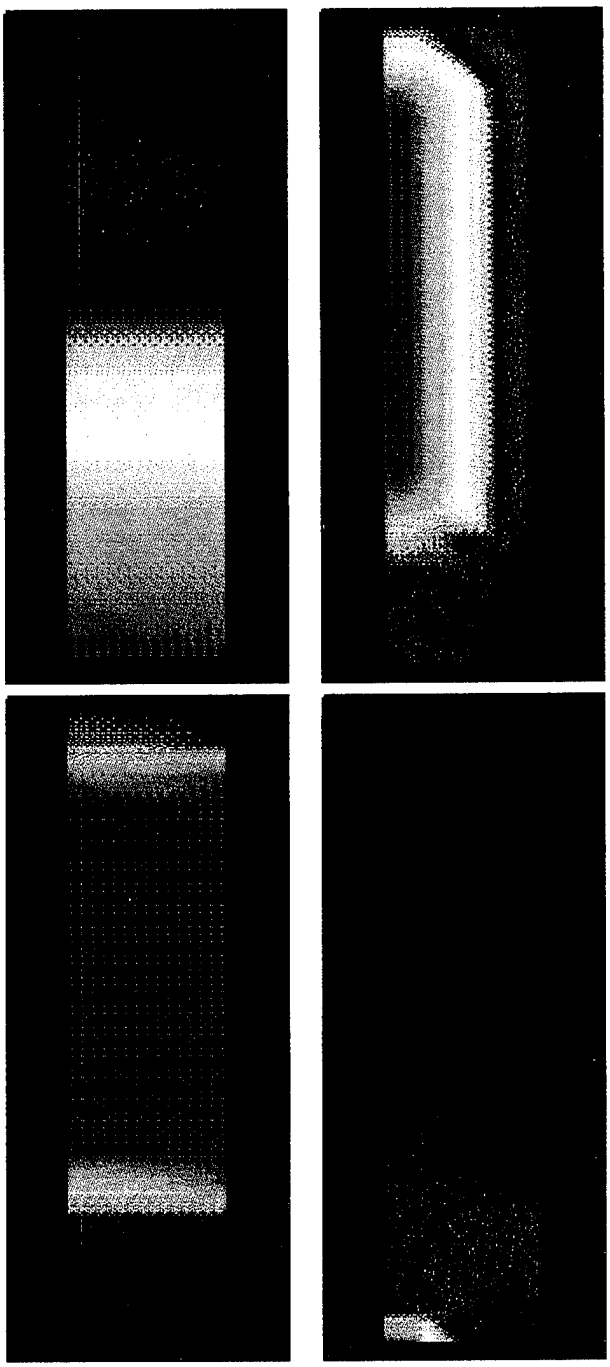

Figure 1. Pressure (upper-left), axial velocity (upper-right), temperature (lower-left), and Precursor mass fraction (lower-right) resulting from the solution of (2.1-9).

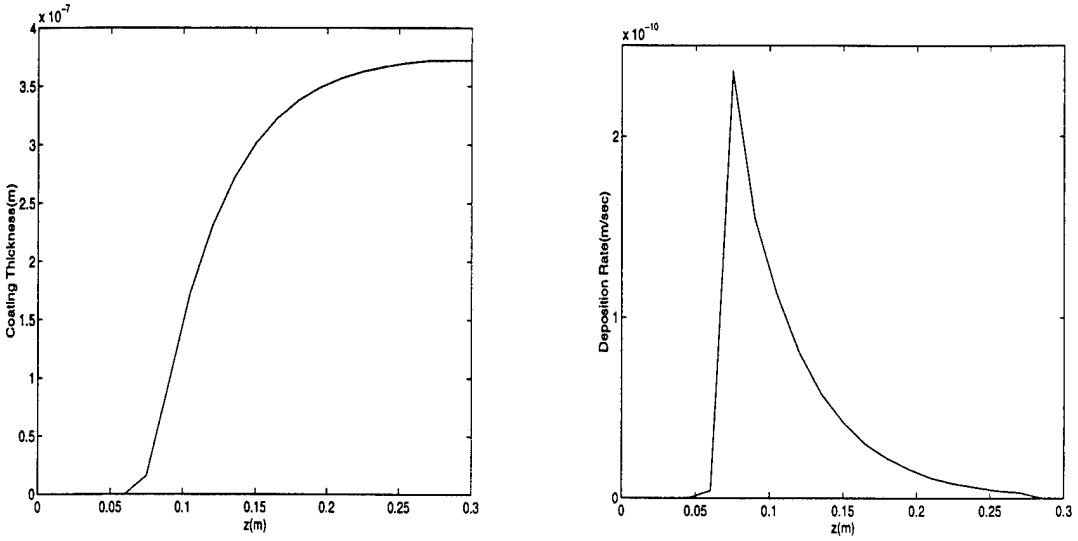

Figure 2. Coating thickness $h(z)$ vs. z on fiber (left), thickness growth rate on wall (right) resulting from solving (2.1-9).

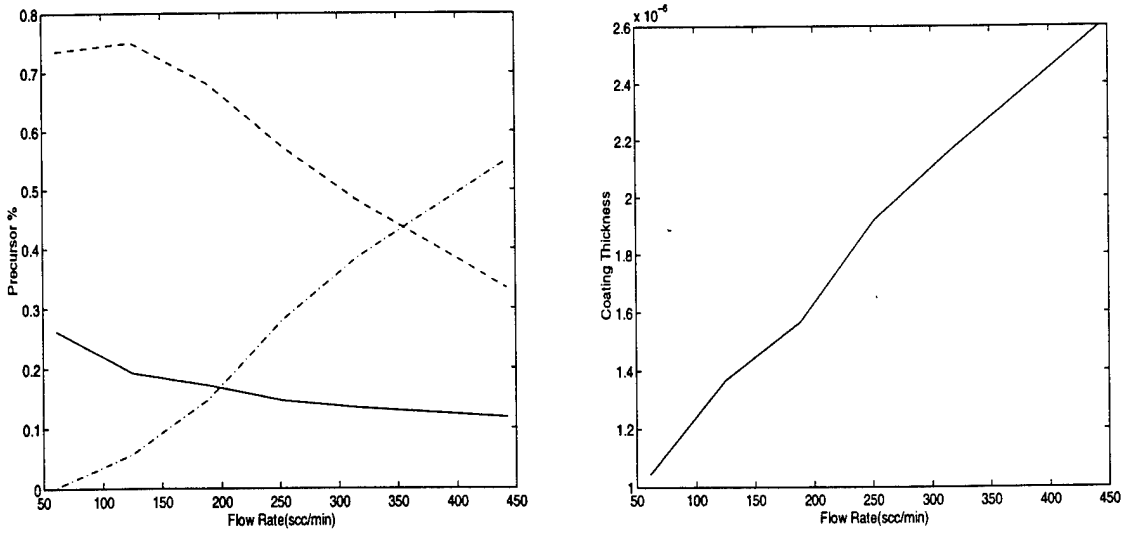

Figure 3. Precursor mass percentage deposited on wall (dashed), fiber (solid), and unreacted (dash-dot) vs. flow rate (left). Coating thickness on fiber vs. flow rate (right) resulting from solving (2.1-2), (2.4-8), (2.10).

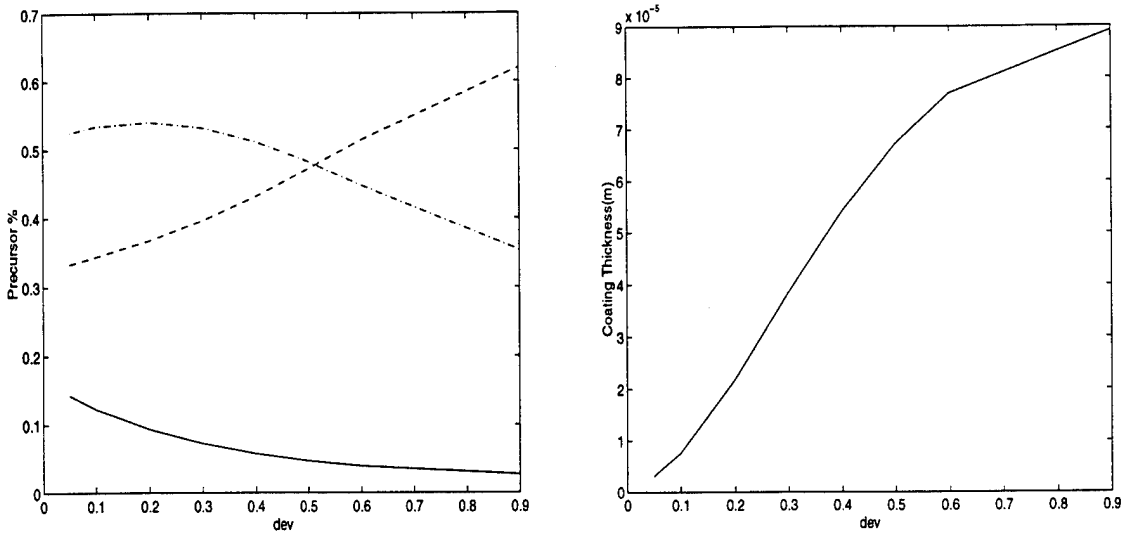

Figure 4. Precursor mass percentage deposited on wall (dashed), fiber (solid), and unreacted (dash-dot) vs. precursor distribution (left). Coating thickness on fiber vs. precursor distribution (right) resulting from solving (2.1-2), (2.4-8), (2.10).

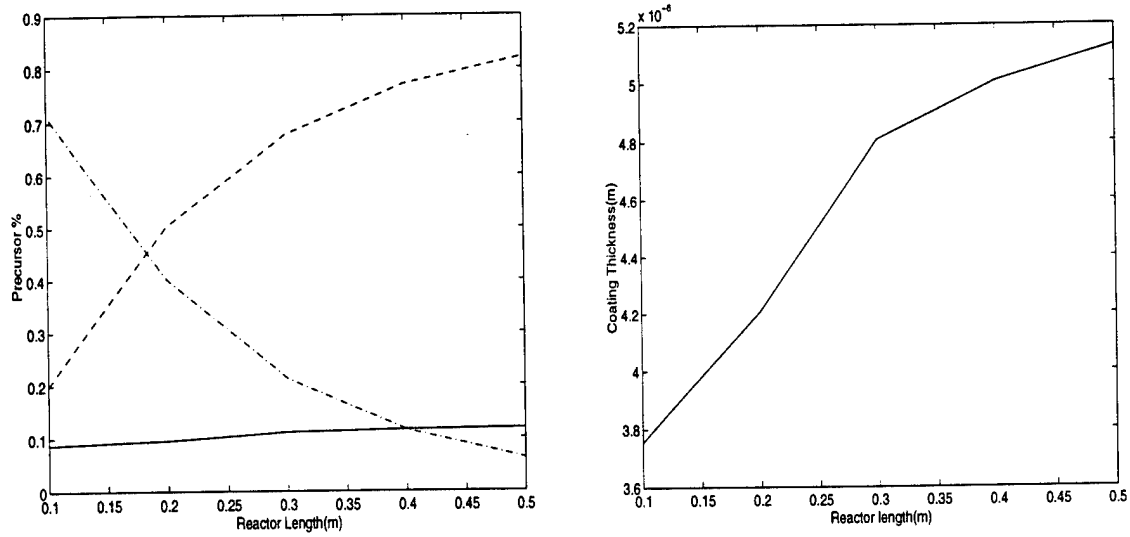

Figure 5. Precursor mass percentage deposited on wall (dashed), fiber (solid), and unreacted (dash-dot) vs. reactor length (left). Coating thickness on fiber vs. reactor length (right) resulting from solving (2.1-2), (2.4-8), (2.10).

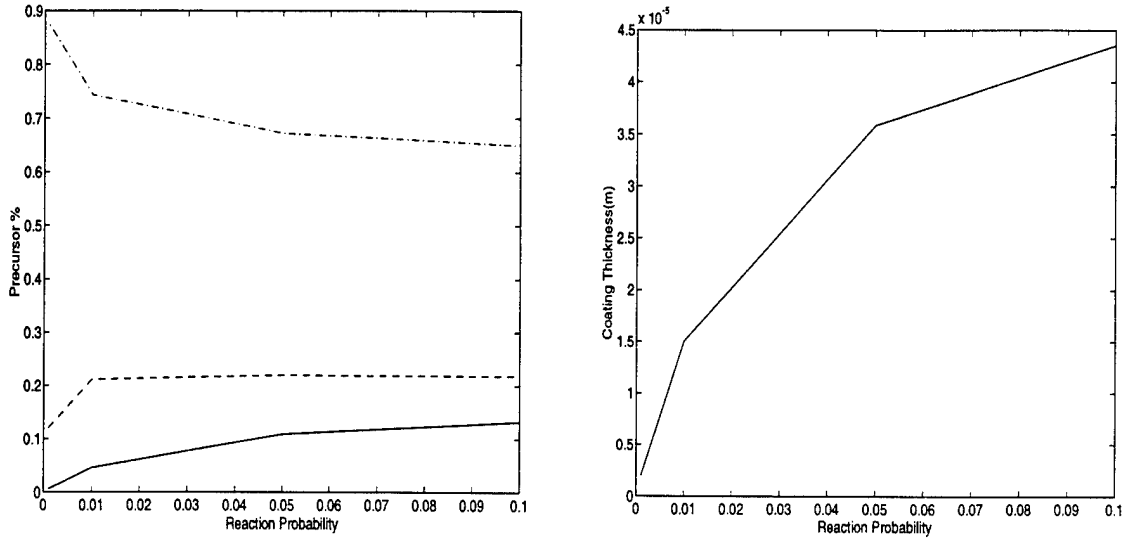

Figure 6. Precursor mass percentage deposited on wall (dashed), fiber(solid), and unreacted (dash-dot) vs. reaction probability α (left). Coating thickness on fiber vs. α (right) resulting from solving (2.1-2), (2.4-8), (2.10).

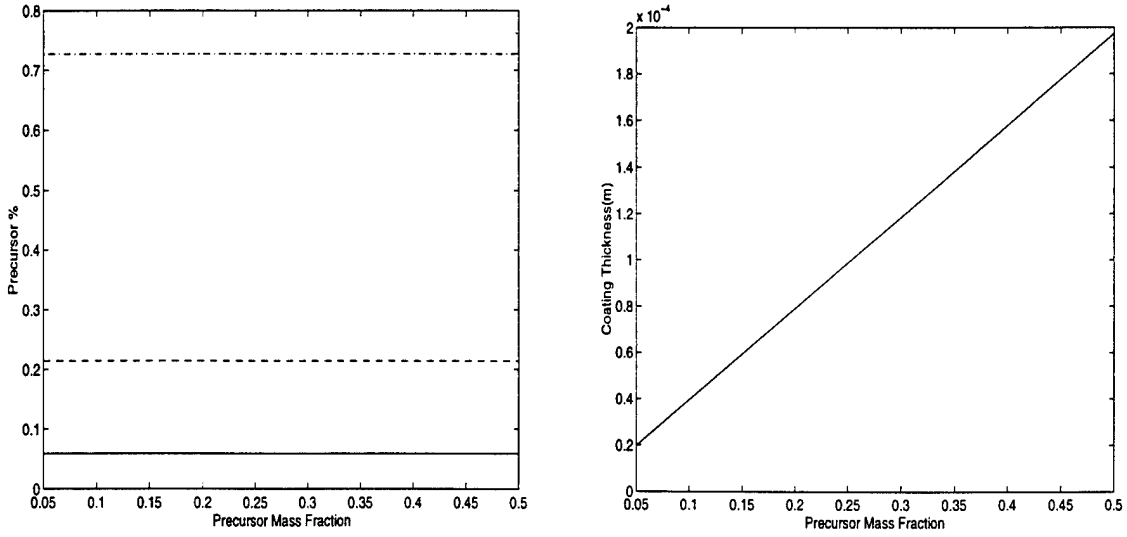

Figure 7. Precursor mass percentage deposited on wall (dashed), fiber (solid), and unreacted (dash-dot) vs. precursor mass fraction (left). Coating thickness on fiber vs. precursor mass fraction (right) resulting from solving (2.1-2), (2.4-8), (2.10).

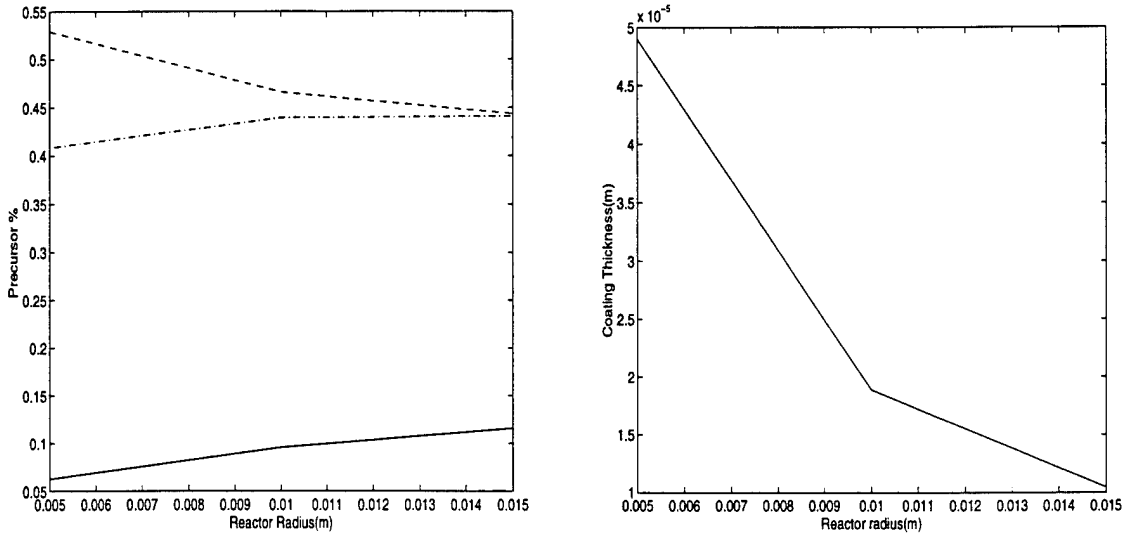

Figure 8. Precursor mass percentage deposited on wall (dashed), fiber (solid), and unreacted (dash-dot) vs. reactor radius (left). Coating thickness on fiber vs. reactor radius (right) resulting from solving (2.1-2), (2.4-8), (2.10).

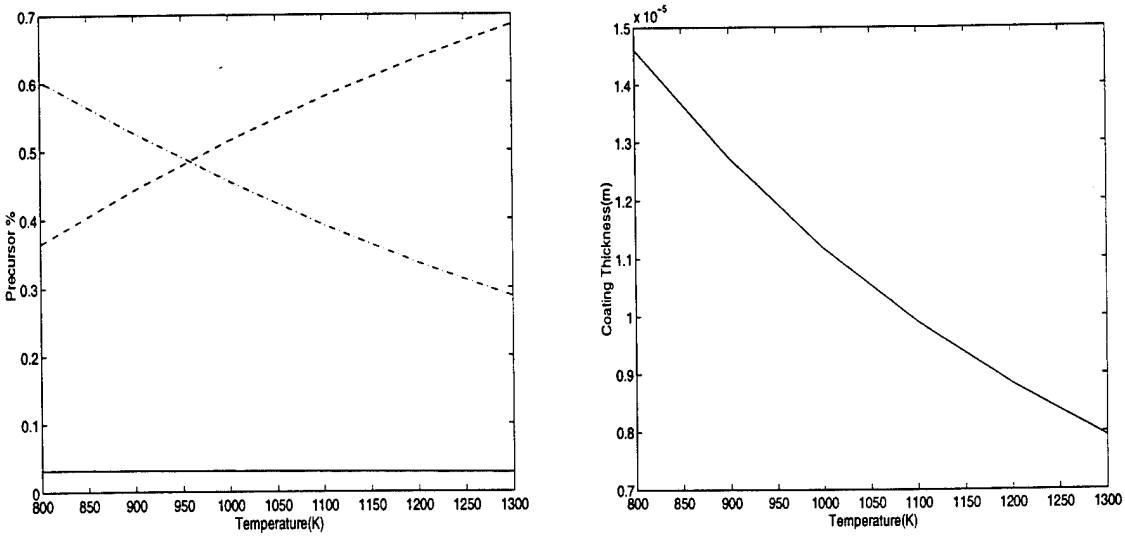

Figure 9. Precursor mass percentage deposited on wall (dashed), fiber (solid), and unreacted (dash-dot) vs. temperature (left). Coating thickness on fiber vs. temperature (right) resulting from solving (2.1-2), (2.4-8), (2.10).

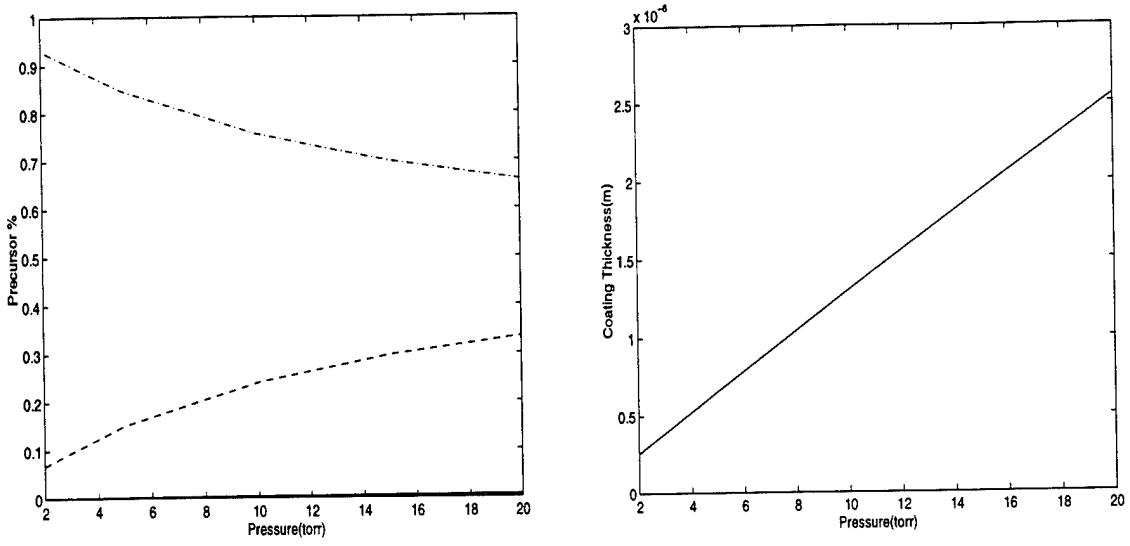

Figure 10. Precursor mass percentage deposited on wall (dashed), fiber (solid), and unreacted (dash-dot) vs. pressure (left). Coating thickness on fiber vs. pressure (right) resulting from solving (2.1-2), (2.4-8), (2.10).

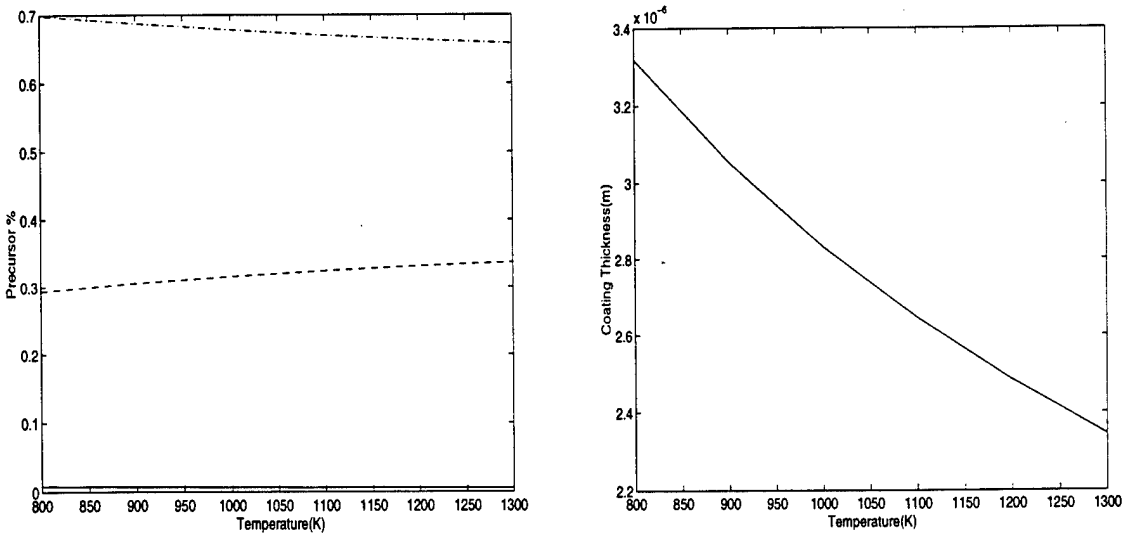

Figure 11. Precursor mass percentage deposited on wall (dashed), fiber (solid), and unreacted (dash-dot) vs. temperature at dwell time = 0.05sec (left). Coating thickness on fiber vs. temperature at dwell time = 0.05sec (right) resulting from solving (2.1-2), (2.4-8), (2.10).

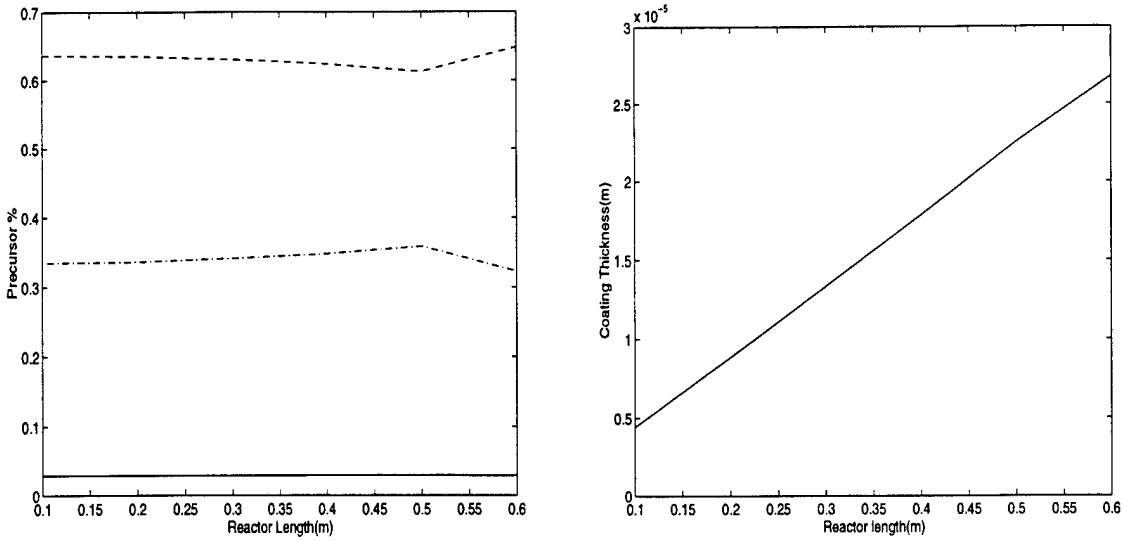

Figure 12. Precursor mass percentage deposited on wall (dashed), fiber (solid), and unreacted (dash-dot) vs. reactor length at dwell time = 0.05sec (left). Coating thickness on fiber vs. reactor length at dwell time = 0.05sec (right) resulting from solving (2.1-2), (2.4-8), (2.10).

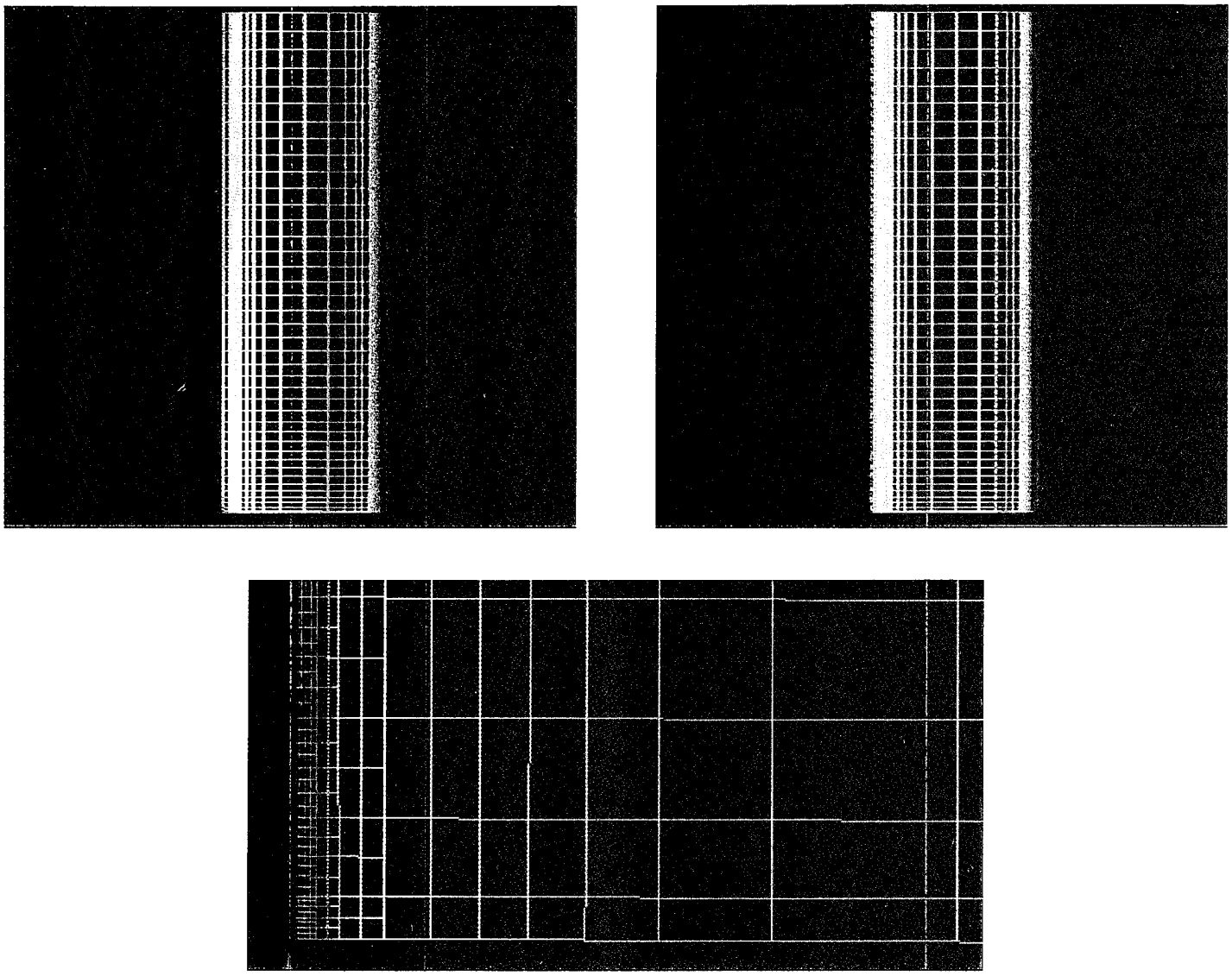

Figure 13. Axial velocity using a 20×20-element graded coarse mesh (top-left), three levels of refinement (top-right), and a blow-up of lower-left corner of top-left of this figure (bottom) resulting from solving (2.1-2), (2.4-8), (2.10).